ELSEVIER

Flexural and shear performance of steel-concrete-steel sandwich slabs under concentrate loads

CrossMark

LengYu-Bing, SongXiao-Bing *

Department of Civil Engineering, Shanghai Jiao Tong University, Shanghai, 200240, PR China

ABSTRACT

This paper studies the flexural and shear performance of steel-concrete-steel (SCS[1]) sandwich slabs. Six simply supported slabs with different shear spans, section depths and steel configurations were tested under concentrate loads applied at the center. After the tests parts of the steel plates were taken off to observe the crack distribution. The observed modes of failure included flexural yielding and shear punching. The former was initiated by tensile yielding of the bottom steel plate, while the latter was primarily due to punching shear failure of the concrete core. After flexural yielding or concrete punching, the carrying capacities could further increase under large deflections, owning to the shear stiffening of the top steel plate and the membrane action of the bottom steel plate. The top steel plate showed significant shear contribution after concrete punching. A theoretical model is developed to predict the resistance of SCS slabs under concentrate loads. The flexural capacity is calculated with the yield-line method, and the punching shear resistance is analyzed with the radial sector model. The shear contribution of the tie bars is also analyzed experimentally and theoretically.

© 2017 Published by Elsevier Ltd.

1. Introduction

1.1. Development of SCS structures

Steel-concrete-steel (SCS) sandwich structures are constructed with the outer steel skins and the concrete core. Composite action is achieved through headed studs, tie bars and other mechanical connectors like angle steel, channel steel, J-hook, etc. [1]. They comprise the advantages of both reinforced concrete (RC) and steel structures, including high bearing capacity, good ductility and integrity, as well as excellent performance in impact resistance and leakage prevention [2]. The steel skins act as both longitudinal reinforcement and permanent formwork, promoting the construction efficiency. In recent years SCS structures have been used in off-shore constructions, submerged tube tunnels, nuclear facilities, bridges, and the application field is still expanding.

During the past 40 years the general performance of SCS structures have been improved greatly with the development of the connection techniques, from the earliest chemical bonding with epoxy [3], to the various mechanical connectors like the overlapped headed studs (in the double skin composite system) [4], the steel bars (in Bi-steel structures) [5], the J-hook connectors [1,6], the channel and steel plate connectors [1]. These connectors attempt to improve the structural performance and construction accessibility, and to enhance the out-of-plane shear and impact resistance. The strength/weight performance is also improved by the use of some innovative ultra-lightweight core materials [1,6].

Various research works have been conducted on SCS specimens, most of which were focused on uniaxial beams, columns and plane shear walls [7–17]. However, two-way slabs are different from beams or columns that forces are transferred in two directions, and both concrete and steel are in tri-axial stress states. It necessarily result in different failure patterns, but research information on SCS sandwich slabs is limited currently. As in practical engineering the SCS panels are usually supported on all four sides and subject to permanent or accidental patch loads, the study of the slab behavior is necessary.

1.2. Research progress on SCS sandwich slabs

Pioneer study on SCS panels was performed by Solomon et al., who proposed the sandwich concept for use in roadway decking and large span bridges in 1976 [3]. In their tests the steel plates were bonded to hardened concrete with epoxy. The specimens failed suddenly by interfacial slippage and separation once concrete was punched through. The strength was not significantly improved yet. Later Shanmugam et al. [18] tested 12 simply supported SCS slabs connected with overlapped headed studs. With a relatively large span/depth ratio (clear span 1400 mm, depth 100 mm), the specimens showed a high degree of

flexural characteristics, and they focused on finite element simulations of the slab behavior.

Sohel et al. [19] carried out tests on eight SCS sandwich slabs with J-hook connectors and ultra-lightweight concrete core, and they concluded that the failure modes and crack patterns were similar to RC slabs. The membrane stretching effect after flexural yielding was considered in their study.

Yan et al. [20–22] conducted tests on 17 SCS slabs with headed stud connectors and ultra-lightweight cement composite, which is proposed to be used in arctic offshore structures to resist ice contact. The investigated parameters included stud spacing, core strength, steel plate thickness, section depth and fiber fraction, and punching shear failure was dominant in their tests. A five-stage load-deflection behavior and two peak resistances were summarized from test results. Analytical models, developed by modifying the code equations from ACI 318-11 and Eurocodes, were developed to calculate both flexural and punching strengths.

1.3. Some classical theories on RC slabs

The force transfer mechanism and failure modes of SCS slabs are in many aspects analogous to that of RC slabs. The strength behavior of RC slabs itself is a complicated problem, so most of the design codes are based on (semi-) empirical equations. But there are also some significant theories revealing the force mechanism in RC slabs. These classical theories are applicable to SCS members after proper modifications.

To deal with flexural yielding failure, the yield-line theory is most widely recognized [23]. Although the upper bound method may give unsafe estimations, it effectively solves the complex problem. As for punching shear failure, some widely used mechanical models include the sector model proposed by Kinnunen et al. [24], and the subsequent critical shear crack theory developed by Muttoni [25,26]. Another method is the upper bound solution based on virtual work equations [27].

Rankine et al. [23] discussed the failure initiation in conventional slab-column specimens, including yielding of the reinforcement (flexure), crushing of the concrete (flexure) and internal diagonal cracking (shear). The failure mechanism is revealed in detail, which helps to understand the slab behavior. Long et al. [28] presented a method for the calculation of punching capacities, based on the elastic thin-plate theory, which described the relationship between the concentrate load and bending moments in the slab. These theories provide powerful insight into the force mechanism in both RC and SCS slabs.

This paper studies the structural behavior of SCS sandwich slabs under concentrate loads through experiments. Based on the observed failure modes and resisting mechanisms, analytical solutions are developed to deal with the carrying capacities of SCS slabs.

2. Experimental investigations

2.1. Test specimens and material properties

Six simply supported sandwich slabs were tested under concentrate loads applied at the center, four of which were typical steel-concrete-steel (SCS) specimens and the other two were steel-concreter (SC²) specimens. Normal concrete with density about 2400 kg/m³ was used as the core material. Fig. 1 depicts the fabrication details of the test slabs. The main purpose was to study the behavior of SCS slabs, and the SC specimens were designed for comparison. In the SCS sandwich assembly shown in Fig. 1(a), the headed studs connected the outer steel plates and the concrete infill, and the round steel bars (also known as tie bars) welded to the steel plates at both ends contributed to vertical shear. Specimens DH-1-4 × 2.35 and DH-1-4 × 3.7 were SC elements, as shown in Fig. 1(b). In these two specimens, the top steel

plate and tie bars were removed, so that the shear contribution of the top steel plate and tie bars can be revealed through direct comparisons with specimens D-1-4 × 2.35 and D-1-4 × 3.7. The shear span/depth ratio λ, referring to the ratio of the clear span (a–b) to the section depth h, ranged from 2.35 to 6.0. Specimen D-1-4 × 6 with $\lambda = 6.0$ was expected to failed in the flexural pattern. Specimen B-1-4 × 3.5 was designed in larger size, so that the deformation shape, failure pattern and crack distribution can be observed more clearly. The specific parameters are listed in Table 1.

Panel assembly was finished in workshop conditions. The studs were welded to the steel plates with a stud welding gun. The steel plates were perforated in advance at the designed positions of tie bars, and the diameter of the holes was slightly larger than the diameter of the tie bars. Then the tie bars passed through the holes and were welded to the steel plates from the outside to form the steel skeleton, as shown in Fig. 2.

The yield and ultimate strengths of the steel plates, studs, tie bars and longitudinal steel bars were obtained from coupon tensile tests. 150 mm concrete cubes were prepared and tested on the same day of the slab tests to obtain the concrete strength. The material properties of steel and concrete are summarized in Table 2.

2.2. Test set-up and measuring scheme

The test device is shown in Fig. 3. The tested panel was simply supported on the rollers on all four sides. The corners were free to lift up. The rollers were supported on rigid steel girders, and the girders were supported on four square columns, so that strain gauges and displacement sensors can be arranged on the bottom surface. The roller supports need to be carefully positioned to ensure the loading to be symmetric in all directions. Square patch load was applied at the center under force control before reaching the first peak resistance, and then transferred to deflection control to obtain the plastic behavior and the descending segment of the load-deflection curves.

During the tests vertical deflections and strains of the steel plates were measured at each load increment. The tensile strains of the tie bars were also tested in specimen B-1-4 × 3.5. The development of the diagonal cracks can be reflected from the tensile strains of the tie bars. Fig. 4 shows the arrangement of the strain rosettes and displacement sensors in specimen D-1-4 × 3.7, as an example.

3. Test results

Typical failure modes of SCS slabs in the tests can be broadly recognized as either shear punching or flexural yielding. Specimen D-1-4 × 6 failed due to flexural yielding, characterized by the global flexural deformation as shown in Fig. 5(a). The upper figure corresponds to the moment of flexural yielding (point 1) on the load-deformation curve in Fig. 7, and the deformation is magnified by 10 times, while the lower figure corresponds to the moment of top steel plate failure (point 2) without magnification. At the flexural yielding moment, the slab showed global flexural deformations except for some local bulge around the load vicinity. The bulge was limited within a distance h from the load perimeter. During the process from point 1 to point 2, yielding of the bottom steel plate initiated from the center and gradually progressed towards the support. At ultimate state, the top steel plate was sheared off, and the bulge was more obvious.

After the test, the steel plate was taken off partially to visualize the concrete cracks, as shown in Fig. 5(b). On the bottom surface, the cracks can be distinguished into tangential and radial cracks. The tangential cracks, or termed as circumferential cracks, developed around the loading vicinity and concentrated near the load vicinity. The radial cracks, on the other hand, extended from the loading region towards the edge, and distributed intensively in the sector region marked in the image. Such a crack pattern was consistent with the theory of radial and tangential moment distributions, as will be explained below.

---

² SC: steel-concrete, with only single steel skin on one side

(a) SCS configuration

(b) SC configuration

1: tie bar; 2: headed stud; 3: concrete; 4: steel plate; 5: longitudinal steel bar, φ10@150 in both directions
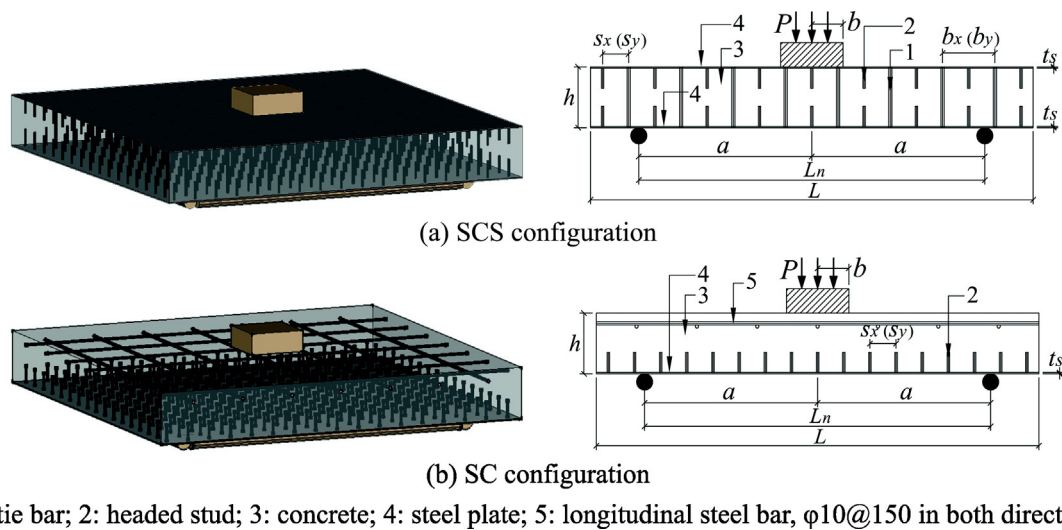
Fig. 1. Fabrication details of the SCS and SC slabs.

Other specimens failed due to local punching, characterized by concrete punching shear cracking and a severe local bulge around the loading region. Yielding of the bottom steel plate was localized around the load vicinity. Fig. 6 shows the typical deformation and failure patterns of specimen B-1-4 × 3.5. The three-dimensional deformed shape of the bottom surface in Fig. 6(b) was measured after testing with a laser displacement sensor. The distance between the bottom surface and the platform of the testing machine was measured at different points. The bottom surface presented a deformation shape like a pan. Specifically, the region within a distance h from the load edge remained plane, and the maximum deformation gradient was located with a distance $h \sim 2h$ from the load edge, as shown in Fig. 6(a). The regions outside the distance $2h$ remained plane without obvious deformations. The deformation of the top surface was concentrated in a small area around the load, and the top steel plate was sheared off along the loading perimeter at last.

After testing the steel plate was also taken off partially to observe the concrete cracks, as shown in Fig. 6(c). On the bottom surface, both tangential and radial cracks were limited within the region with a distance $2h$ from the loading perimeter, and the region with a distance of $h–2h$ from the load cracked most seriously. The tangential cracks were generally wider than radial cracks. The slab was cut into two pieces at last to observe the internal crack pattern. From the side view, the critical shear crack, which formed the surface of the concrete punching cone, inclined about 26°–30° to the slab plane.

Fig. 7 shows the load-deflection curves of all the test slabs. The deflections were measured at the midpoint under the load. For the SCS slabs failed by punching, there were two critical points during the failure process. At the first turning point (the triangular points in the curves) the concrete was punched through, thus the punching cone was formed. The bottom surface began to bulge outward. After concrete

punching, the capacity of specimens D-1-4 × 2.35 and B-1-4 × 3.5 remained stable, but in specimen D-1-4 × 3.7 the capacity dropped slightly. In both cases the carrying capacity increased again under large deflections, owning to the shear contribution of the top steel plate and the membrane action of the bottom steel plate. The second turning point (the circular points in the curves) corresponded to the ultimate carrying capacity after which the top steel plate was sheared off along the loading perimeter, with a loud noise.

In the SC slabs, on the contrary, failure was sudden without any warning once concrete was punched. Without the contribution from the top steel plate and tie bars, the carrying capacity dropped immediately after punching occurred, showing a sharp turning point on the load-deflection curves. The residual capacity was provided totally by the shear and membrane action of the bottom plate thereafter. It was far smaller than that of the SCS slabs. The top surface remained flat and uncracked outside the loading perimeter.

The response of specimen D-1-4 × 6, which is prone to flexural failure, also shows two turning points: the moments of flexural yielding and ultimate failure. The bottom steel plate began to yield near point 1. From point1 to point 2 the yielded region extended outward, until the top steel plate was sheared off at point 2.

4. Analytical study on failure modes and strength of SCS slabs

4.1. General behaviors of flexural and shear failures

The failure of SCS sandwich slabs under concentrate loads can be classified broadly as flexural yielding and shear punching, besides the potential local damage patterns like local crushing of concrete, local buckling of the top steel plate and interfacial slippage. The local damage patterns are not considered in this study. Flexural failure initiates from

Table 1
Parameters of the SCS slabs.

Specimen	λ	h (mm)	t_s (mm)	L_n (mm)	L (mm)	Loading area	Tie bar[a]	Headed stud[b]	Construction type
D-1-4 × 2.35	2.35	150	3.05	860	1100	155 × 155	φ9.6@130 × 130	φ6@65 × 65	SCS
D-1-4 × 3.7	3.7	150	3.05	1260	1500	155 × 155	φ9.6@130 × 130	φ6@65 × 65	SCS
DH-1-4 × 2.35	2.35	150	3.05	860	1100	155 × 155	\	φ6@65 × 65	SC
DH-1-4 × 3.7	3.7	150	3.05	1260	1500	155 × 155	\	φ6@65 × 65	SC
B-1-4 × 3.5	3.5	300	6.0	2400	2840	300 × 300	φ9.6@220 × 220	φ13@110 × 110	SCS
D-1-4 × 6	6	150	3.05	2100	2400	300 × 300	φ9.6@130 × 130	φ6@65 × 65	SCS

Notes: (a) the symbols of the tie bars $\varphi d_v@b_x \times b_y$: d_v = diameter of the steel bars, b_x & b_y = bar spacing in two directions; (b) the symbols of headed studs $\varphi d_s@s_x \times s_y$: d_s = diameter of the studs, s_x & s_y = stud spacing in two directions.
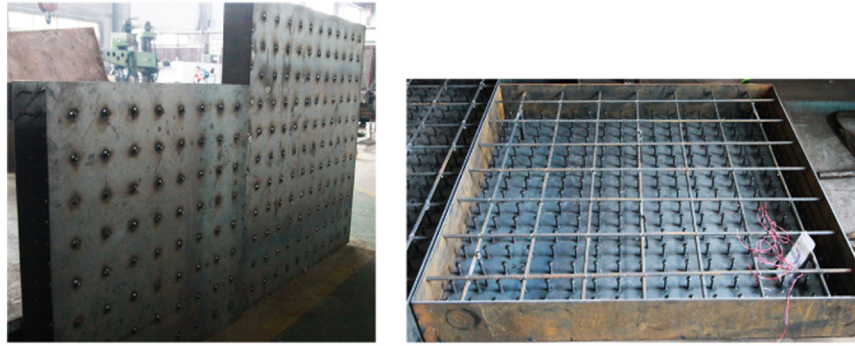
Fig. 2. The steel skeleton.

tensile yielding of the bottom steel plate, while punching shear failure is characterized by punching of the concrete core around the concentrate load. The general load-deflection behaviors of the two failure patterns are described in Fig. 8.

Flexural failure usually occurs in slender slabs or slabs with relatively low steel ratios. In the flexural failure process [Fig. 8(a)], the bottom steel plate begins to yield around point 1, which is the end of the linear segment. Then the yielded region spreads outward from the center, while the carrying capacity remains stable. The capacity increases again from point 3, due to shear stiffening and membrane action of the steel plates until point 4, when the top steel plate is sheared off along the loading perimeter. Flexural failure is characterized by considerable yielding of the bottom steel plate prior to punching, as well as the global flexural deformation, although some local bulge may also exist around the loading region.

Punching shear failure, which is usual predominant in thick slabs, or slabs with relatively high steel ratios, also experiences the linear stage 0–1, and non-linear stage 1–2, as shown in Fig. 8(b). At point 2 when punching occurs in the concrete core, the bottom steel plate may have yielded around the loading region, but it is not a necessary condition. It constitutes a significant difference from the flexural failure. There are two possibilities after point 2. The carrying capacity may drop slightly, but in slabs with relatively large steel ratios or enough tie bars, it shows a stable platform instead. The carrying capacity increases again from point 3, due primarily to shear stiffening of the top steel plate, and membrane action of the bottom steel plate. Meanwhile, with the development of the inclined cracks, the contribution of the tie bars also increases. The noises of tie bar fracture were heard successively in the tests, but it did not affect the overall upward trend of the curve. At point 4 the top steel plate is shear fractured. Punching shear failure is characterized by concrete punching shear cracking and the local bulge around the loading region after point 2. Yielding of the bottom steel plate and deformation are more localized, and no obvious deformation is measured outside the punching cone from the bottom surface.

The SCS slabs exhibit excellent ductile performance during both flexural and punching failure processes. But in SC slabs the situation is quite different when concrete is punched through. The immediate unloading behavior indicates that the top steel plate plays a significant role after core punching.

In the tested SCS slabs, the ultimate capacities at point 4 (P_u) all exceeded the punching load at point 2 (P_{cr}), but not necessarily. For example, the punching strength P_{cr} can be promoted by reducing the shear span/depth ratio, but the ultimate strength P_u, which relies mainly on the top steel plate strength, is not influenced directly. The two capacities depend on different resisting mechanisms. But it is suggested that letting P_u exceeding P_{cr} should be an effective way to ensure ductility of the structure during the punching failure process.

The flexural and shear resistances together (the lower one) decide the carrying capacities of SCS slabs. Besides geometrical conditions like sizes of the concentrate load and shear span/depth ratios, the failure behavior is also influenced by other factors like concrete strength, steel plate ratio, tie bar strength, etc.

From the view of practical engineering, the most critical capacities are the first turning point: the flexural yielding strength P_f and the punching strength P_{cr}. The ultimate capacity P_u, which results from shear stiffening and membrane action of the outer steel plates under fairly large deflections, can be regarded as a safety reservation, or it may be considered under extreme loads.

Table 2
Material properties of concrete and steel (N/mm², mean value).

Specimen	Concrete	Steel plate		Tie bar		Longitudinal steel bar		Stud
	f_c	f_y	f_u	f_{yv}	f_{uv}	f_{ys}	f_{us}	f_{stu}
D-1-4 × 2.35	29.8	305	455	360	520	\	\	480
D-1-4 × 3.7	29.8	305	455	360	520	\	\	480
DH-1-4 × 2.35	29.8	305	455	\	\	455	620	480
DH-1-4 × 3.7	29.8	305	455	\	\	455	620	480
B-1-4 × 3.5	31.9	280	440	360	520	\	\	520
D-1-4 × 6	31.9	305	455	360	520	\	\	480

Notes: f_c = concrete compressive strength; f_y (f_u) = yield (ultimate) strength of the steel plates; f_{yv} (f_{uv}) = yield (ultimate) strength of the tie bars; f_{ys} (f_{us}) = yield (ultimate) strength of the longitudinal steel bars,; f_{stu} = strength of the studs (hardened steel without definite yield point).
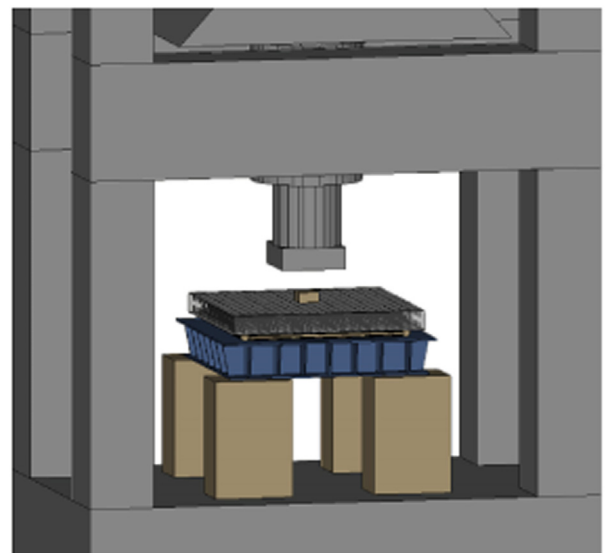

Fig. 3. The test device.

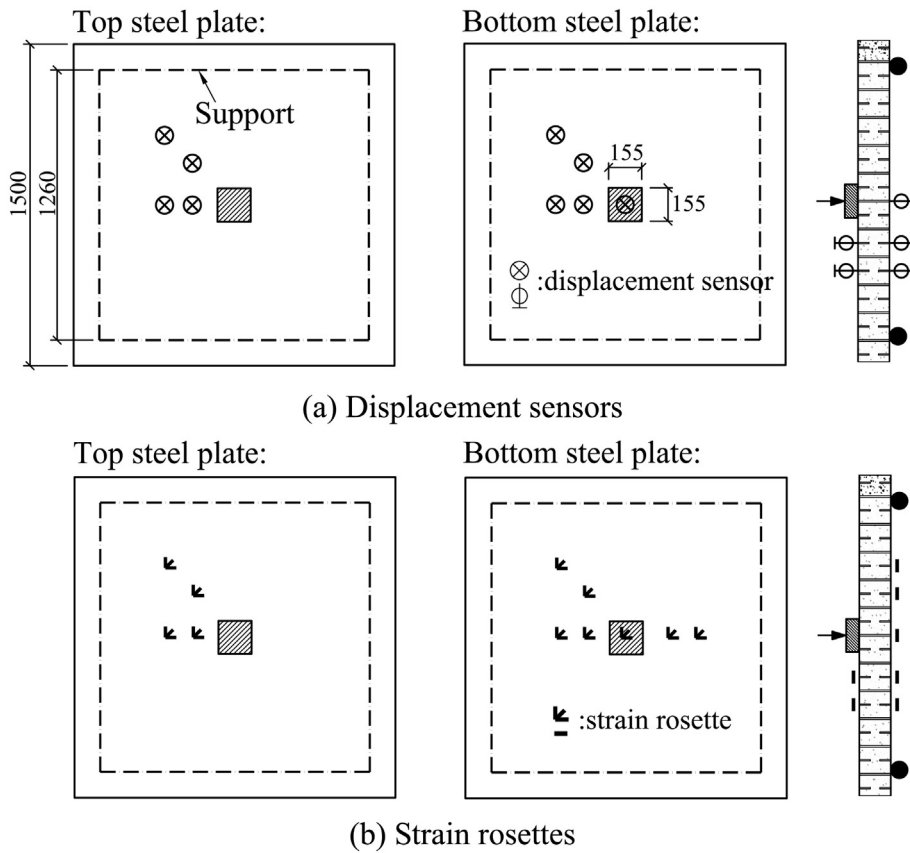(a) Displacement sensors

(b) Strain rosettes

Fig. 4. The measuring scheme in specimen D-1-4 × 3.7.

4.2. Moment distributions in two-way slabs

The punching shear strength depends on the combined effect of the shear forces and bending moments in the vicinity of the loading region [28], so it is necessary to discuss the moment distribution in slabs. Before flexural failure, the bottom steel plate has not yielded extensively. Specifically, the yielded region is limited around the load periphery, and outside this region it is still in the elastic range. Therefore, an elastic solution can be used to calculate the bending moments in the slab before flexural failure. The values of the radial and tangential bending moments are obtained from the thin-plate theory [28].

$$M_r = \frac{P}{8\pi}\left[2(1+\nu)\log\left(\frac{a}{r}\right) + A(1+\nu)\left(1 - \frac{a^2}{r^2}\right) + 2B(1-\nu)\left(\frac{1}{r^2} - \frac{1}{a^2}\right)\right] \tag{1a}$$

$$M_t = \frac{P}{8\pi}\left[2(1+\nu)\log\left(\frac{a}{r}\right) + 2(1+\nu) + A(1+\nu)\left(1 + \frac{a^2}{r^2}\right) - 2B(1-\nu)\left(\frac{1}{r^2} + \frac{1}{a^2}\right)\right] \tag{1b}$$

where

$$A = \frac{2b^2}{\left(a^2 - b^2\right)}\log\left(\frac{a}{b}\right) \tag{1c}$$

$$B = \frac{a^2 b^2\left[(1-\nu)\left(\frac{a^2}{b^2} - 1\right) + 2(1+\nu)\frac{a^2}{b^2}\log\left(\frac{a}{b}\right)\right]}{(1-\nu)\left(a^2 - b^2\right)\left[(1+\nu)\frac{a^2}{b^2} + 1 - \nu\right]} \tag{1d}$$
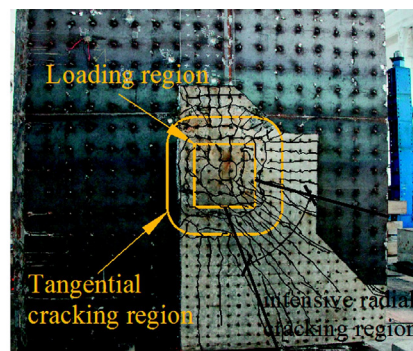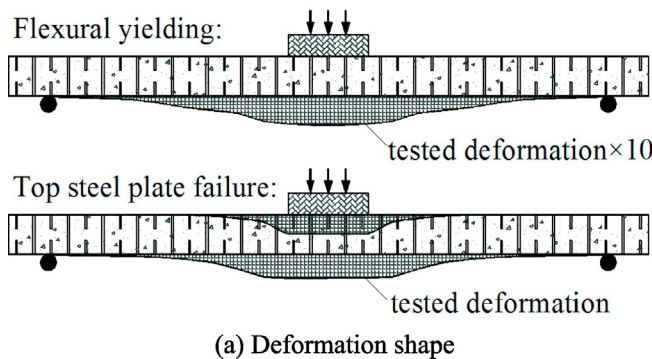

(a) Deformation shape

(b) Concrete cracks on the bottom surface

Fig. 5. Deformation and crack distribution in specimen D-1-4 × 6.

critical punching shear crack ↓↓↓ shear failure of top steel plate

h h
$2h$ $2h$ maximum deformation gradient

(a) Deformation shape from the side view

(b) 3D mapping of the bottom surface at failure

Loading region

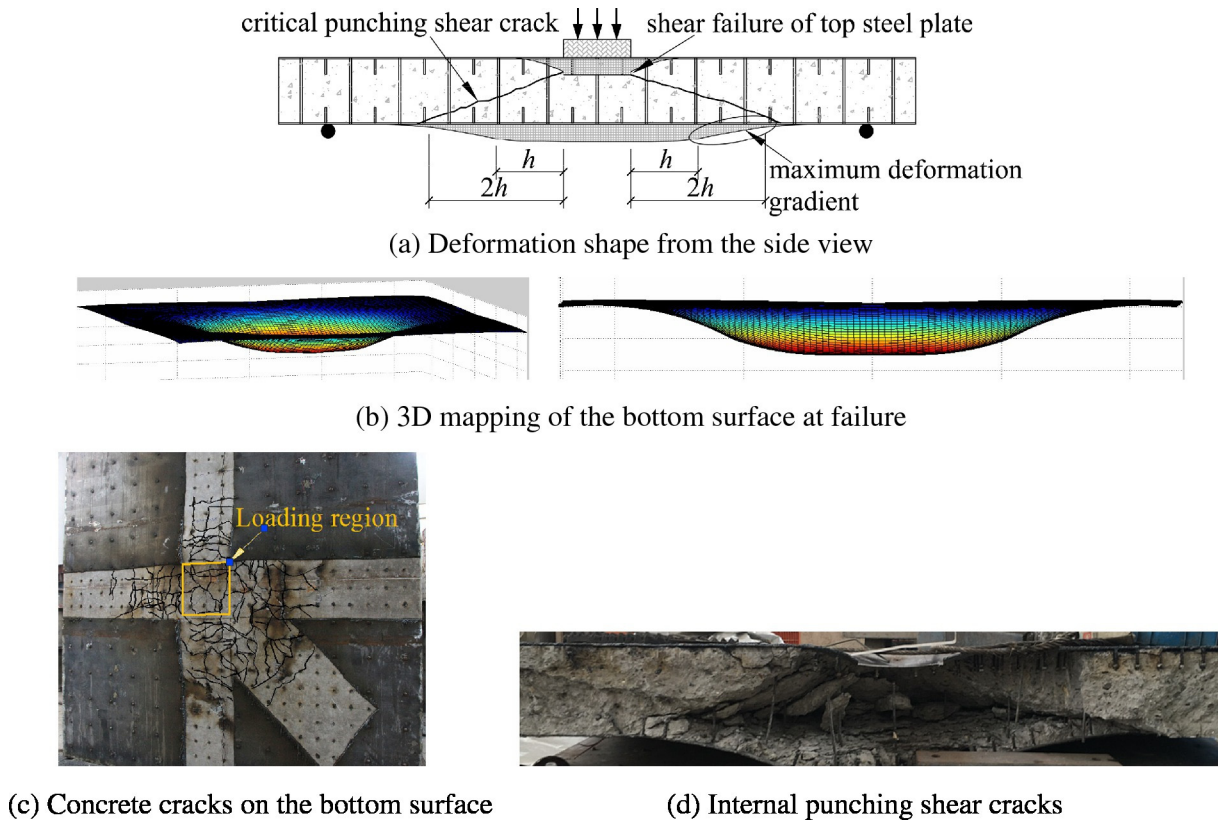(c) Concrete cracks on the bottom surface   (d) Internal punching shear cracks

Fig. 6. Deformation and crack distribution in specimen B-1-4 × 3.5.

The meanings of P, a, b and r are shown in Fig. 9, and ν is the Poisson's ratio. The theory is derived on circular simply supported slabs subjected to circular patch loads applied at the center. Both geometrical and loading conditions are axis-symmetric. When applied to square slabs, a can be taken as the distance between the center of the patch load and the support, and b as half the size of the loading region.

The elastic theory indicates that the radial moments are high at the load vicinity, but decrease rapidly as the radius increases. The tangential moments, by contrast, decrease slowly from the center to the support, with small gradients. This explains why in specimen D-1-4 × 6 the tangential cracks concentrated near the loading region while the radial cracks extended from the loading region towards the edge.
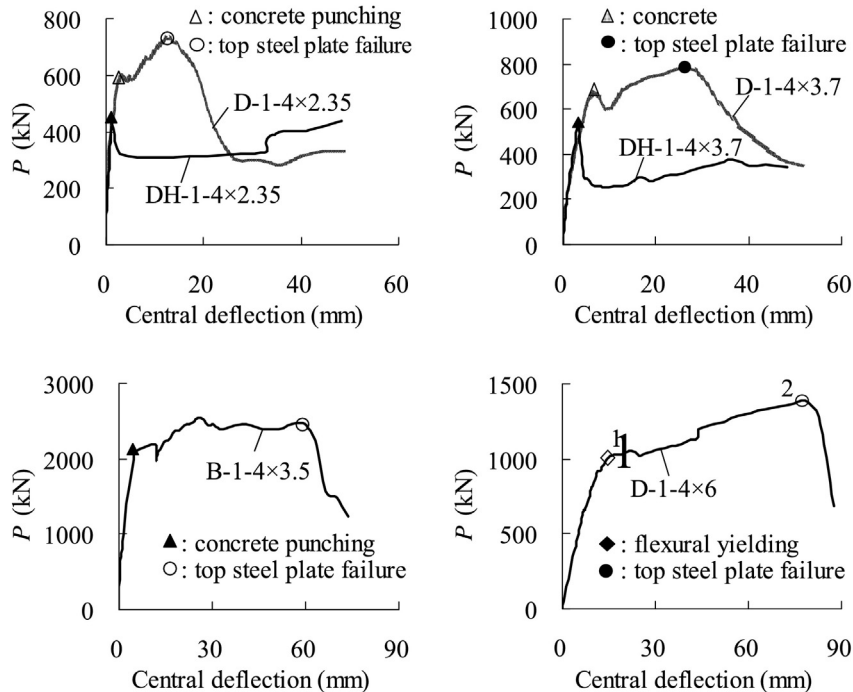
Fig. 7. Load-deflection responses.

(a) Flexural failure   (b) Punching shear failure
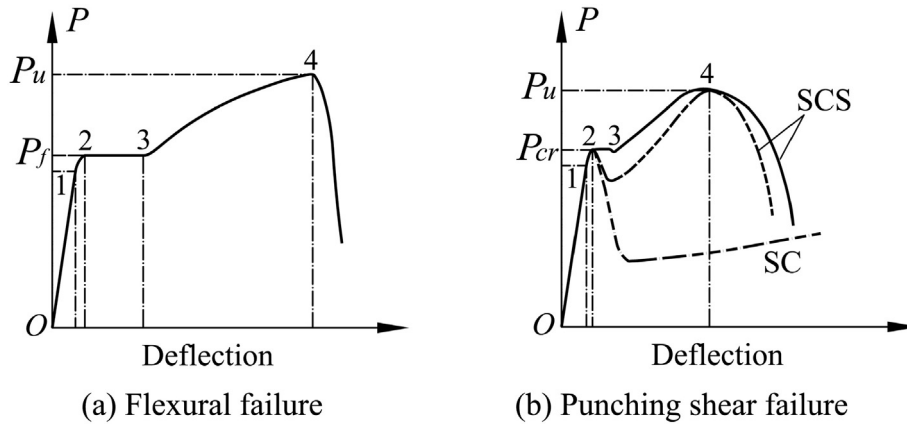
Fig. 8. General load-deflection behaviors of flexural and punching shear failures.

The accuracy of the theory can be verified by comparing the theoretical and measured tensile strains of the bottom steel plate in specimen D-1-4 × 6. The tested strains obtained from the strain rosettes are converted into the tangential strains ε_{st} and radial strains ε_{sr}. The tangential and radial directions, as shown in Fig. 10(a), are related to the critical punching perimeter proposed by Eurocode 2 [29]. Although the exact position of the critical perimeter (with a distance 2h from the edge of the load as suggested by Eurocode 2) is still questionable, the shape is confirmed in the tests, as well as in previous studies [19]. The tangential direction at a point is defined as the direction parallel to the critical perimeter, while the radial direction defined as the direction perpendicular to the critical perimeter.

The radial and tangential bending moments per unit length in the slab under the concentrate force P are calculated according to Eqs. (1a), (1b), (1c) and (1d). Dividing the bending moments by the flexural lever arm, thickness and elastic modulus of the steel plate gives the theoretical values of the steel strains. The flexural lever arm is approximated to be 0.9h [17]. The comparisons between the theoretical and experimental steel strains in Fig. 10(b) show that the elastic thin-plate theory can estimate the steel strains with enough accuracy. The initial deviation is believed to result from the rough estimation of the lever arm. The results are acceptable for engineering calculations before steel plate yielding.

4.3. Flexural capacity P_f

The yield line mechanism in Fig. 11(a) describes well the flexural deformation pattern and crack distribution in specimen D-1-4 × 6, especially the intensive radial cracks in the sector region. It is also confirmed in Ref. [23] that such a yield line mechanism gives the most reasonable solution of the flexural capacities for conventional slab-column specimens.

For slabs simply supported along all four edges, the assumed yield lines divide the slab into two types of rigid bodies, I and II, as shown in Fig. 11(a). Part I is supposed to rotate around the support. But in part II the two supports intersect at the corner, so that the sector is
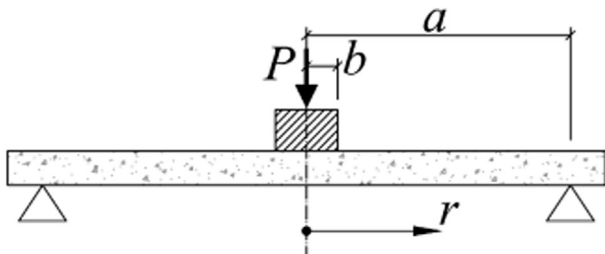

Fig. 9. Axis-symmetric slab under concentrate loading.

difficult to rotate around both supports simultaneously. The shaded areas in Fig. 11(b) act as rigid blocks to prevent any local deformations. Consequently, part II can only rotate around the virtual supports across the corners. After the formation of yield lines A and B, the slab becomes a mechanism due to overall yielding. Under this yield line pattern, the flexural capacity can be obtained from the virtual work principle [23].

Yield line A, which develops from the corner of the load towards the intersection of the axes of rotation, is supposed to form an angle α with the vertical direction, as shown in Fig. 11(b). Under unit downward deformation at the loading point, the energy dissipation in yield line A is

$$W_A = m_f \left[\frac{s-b}{\cos\alpha} \cdot \sin\left(45^\circ - \alpha\right) \Big/ \frac{a-b}{\cos\alpha} \cdot \cos\left(45^\circ - \alpha\right) \right] + m_f[(s-b)\tan\alpha/(a-b)]$$
$$= m_f \frac{s-b}{a-b}\left[\tan\left(45^\circ - \alpha\right) + \tan\alpha \right] \tag{2}$$

And the energy dissipation in yield line B is

$$W_B = m_f \frac{2b}{a-b} \tag{3}$$

m_f is the flexural strength of the slab per unit length with $m_f \approx f_y t_s \cdot 0.9h$.

According to the virtual work principle:

$$P_f = 8m_f \left[\frac{s-b}{a-b}\left[\tan\left(45^\circ - \alpha\right) + \tan\alpha \right] + \frac{b}{a-b} \right] \tag{4}$$

The partial deviation of α in Eq. (4) shows that when $\alpha = 22.5°$, P_f reaches the minimum value:

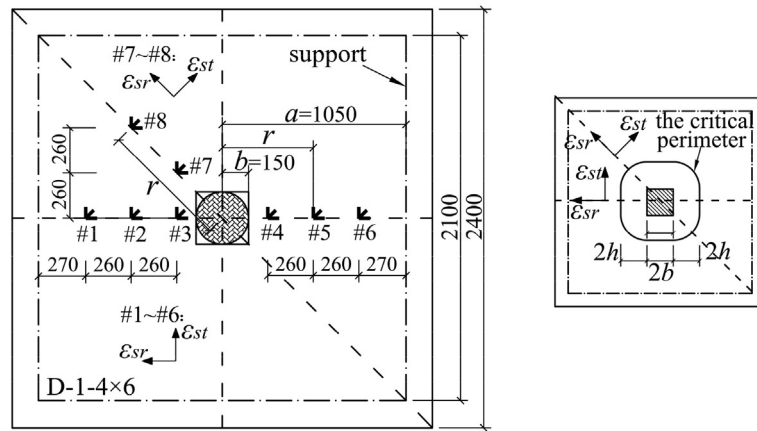$$P_{f,\,min} = 8m_f \left(\frac{s}{a-b} - 0.172\frac{s-b}{a-b} \right) \tag{5}$$

As $\frac{s-b}{a-b} \approx 1$, the flexural capacity P_f can be approximated as

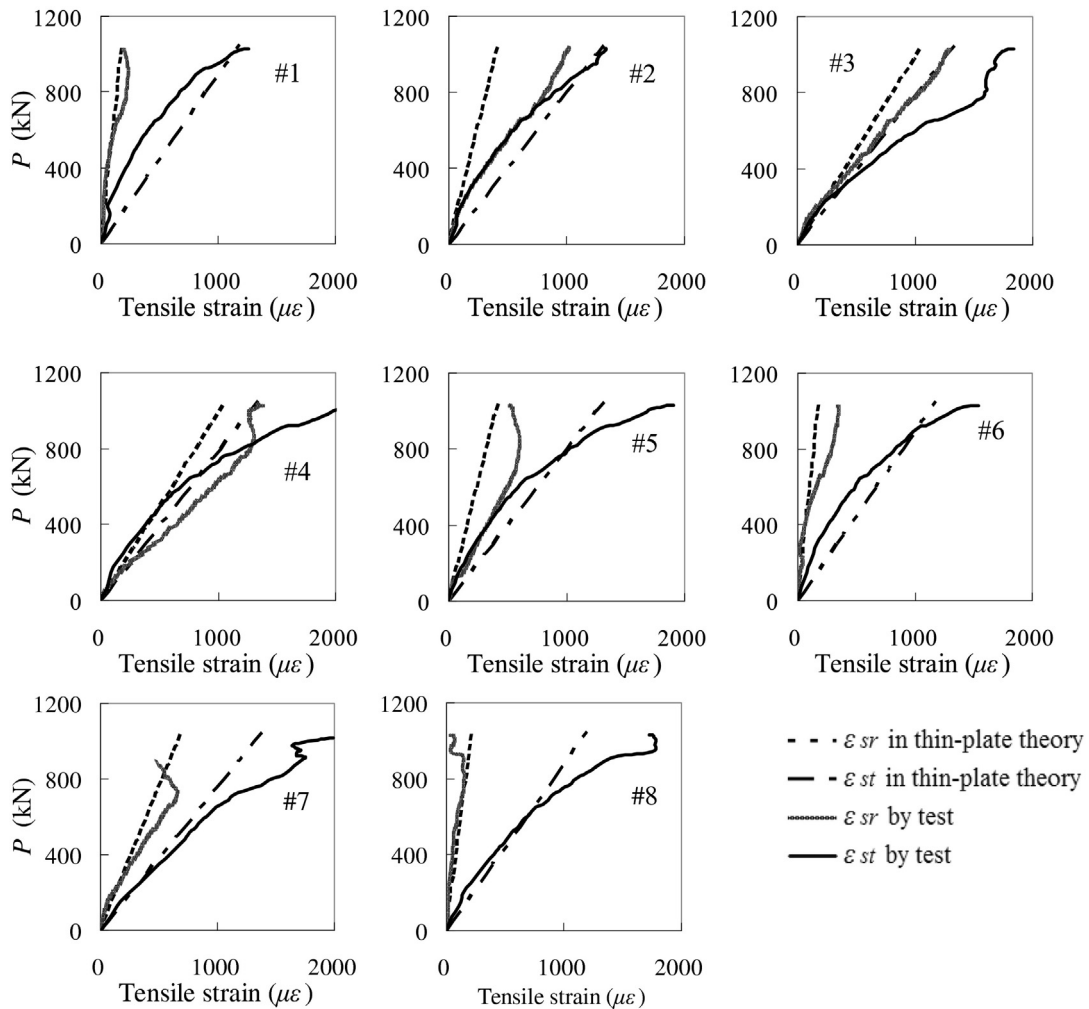$$P_f \approx 8m_f \left(\frac{s}{a-b} - 0.172 \right) \tag{6}$$

The flexural capacity is minimized when the load is applied at the very center, as the case in Fig. 11, thus Eq. (6) actually gives the minimum value of flexural capacities of two-way slabs under concentrate loads, among all upper bound solutions.

4.4. Punching shear capacity P_{cr}

Punching shear failure is characterized by the formation of the concrete critical punching crack, and the punching cone around the periphery of the loading. The punching strength P_{cr} is dependent on the stress

(a) Layout of the strain rosettes on the bottom steel plate

(b) Theoretical and experimental tensile strains of the bottom steel plate

Fig. 10. Comparisons of the theoretical and experimental steel strains of the bottom steel plate in specimen D-1-4 × 6.

state and strength of concrete at the critical region. The tie bars also contribute to the punching strength. During the analysis process, the following conditions are considered.

i) The model considers only ordinary slabs with shear span/depth ratio larger than 2.0. In deep members the force mechanism is dependent on the diagonal compression effect, or termed as strut effect, just like the differences between slender and deep beams. The behavior of deep slabs should be considered specially.

ii) Analysis is based on an axis-symmetric model, which seems to be idealized but typical. The punching shear capacity is minimized when the load is applied at the very center.

4.4.1. Failure criteria of concrete

Selecting a failure criterion is the first step to study the concrete behavior. The failure process of concrete is complicated, and many failure criteria are available [30], from the simplest maximum tensile stress
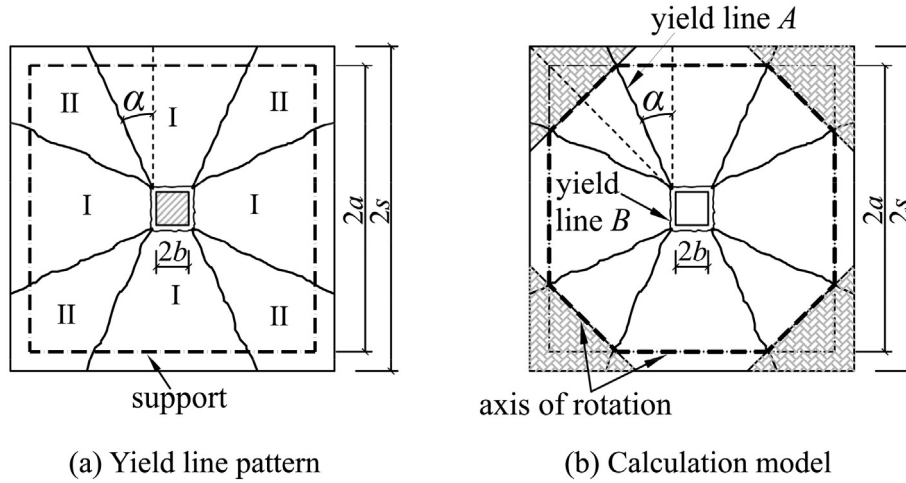
(a) Yield line pattern   (b) Calculation model

Fig. 11. Yield line pattern in SCS sandwich slabs.

criterion and maximum tensile strain criterion with only one parameter, to the Mohr-Coulomb and Drucker-Prager criteria with two parameters, and Willam-Warnke criteria with three or five parameters. With additional parameters, accuracy is improved but the complexity is also increased inevitably. Considering both simplicity and effectiveness, the Mohr-Coulomb criterion with tension cut-off [30] is adopted. This combined criterion has modified the original Mohr-Coulomb criterion which overestimates the tensile capacity of concrete. It describes the two potential failure patterns in concrete, i.e., tension and shear, with simple expressions and adequate accuracy.

Tension failure happens when the principal stress reaches the tensile strength f_t:

$$\max(\sigma_1, \sigma_2, \sigma_3) = f_t \tag{7}$$

As the principal stresses are usually expressed with $\sigma_1 \geq \sigma_2 \geq \sigma_3$, the cut-off criterion, which is also well known as the Rankine criterion, can be expressed directly as:

$$\sigma_1 = f_t \tag{8}$$

The Mohr-Coulomb criterion, on the other hand, describes the relationship between normal and shear stresses on the failure surface when shear failure happens:

$$|\tau| = c - \sigma \tan\phi \tag{9}$$

where c is the cohesive strength and φ is the friction angle of concrete. The normal stress is positive in tension.

The stress state and failure criteria under the interaction of normal stress σ and shear stress τ are shown in Fig. 12. A critical stress state exists that reaches both Mohr-Coulomb and Rankine failure criteria [30]. At the critical stress state the concrete crack is just at the transition between the open tensile crack and closed shear crack, so that the normal stress at the failure surface is zero. The Mohr circle of critical stress state is tangent to the two failure criteria simultaneously, and the tangent point with the Mohr-Coulomb criterion is $(0, c)$. Based on this geometric relationship, the material parameters c and $\tan\varphi$ are obtained [31]:

$$c = \sqrt{\frac{f_c f_t}{2}} \tag{10}$$

$$\tan\phi = \frac{\sqrt{2}}{4} \frac{f_c - 2f_t}{\sqrt{f_c f_t}} \tag{11}$$

For two-way slabs subjected to a concentrate load, the loading region is a critical location of both maximum shear and bending moment. The concrete in the shear-compression zone are under three-dimensional stress state, as shown in Fig. 13. But according to Eqs. (1a), (1b), (1c) and (1d), in this central region, the radial moment M_r is far larger than the tangential moment M_t, so that the radial stress σ_{c1} and shear stress τ_c are critical, and the tangential stress σ_{c2} is just a secondary stress. The three-dimensional stress condition can thus be simplified into a plane stress state. The planar failure envelopes under the interaction of a normal stress σ_c and a shear stress τ_c are applicable.

When tension failure occurs in concrete, the Mohr circle is tangent to the Rankine criterion as shown in Fig. 14(a), and the critical stress state
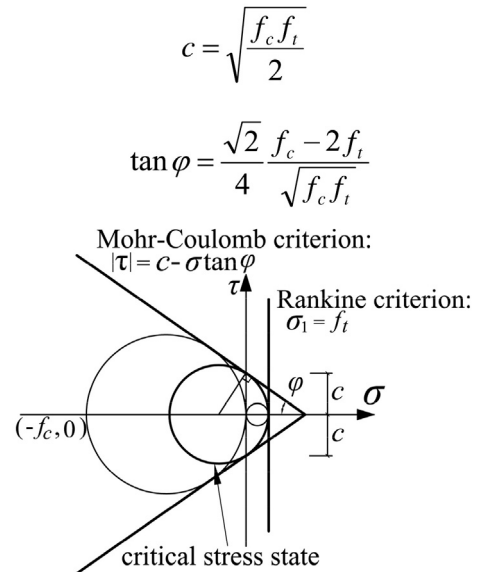

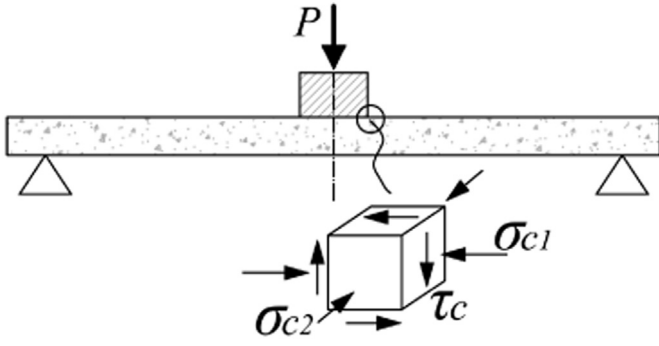**Fig. 12.** Failure criterion of concrete and the Mohr circle of critical stress state.

Fig. 13. Concrete stress state in the critical regions.

is:

$$\sqrt{\left(\frac{\sigma_c}{2}\right)^2 + (\tau_c)^2} + \frac{\sigma_c}{2} = f_t \tag{12}$$

In Eq. (12) the values of σ_c and τ_c constitute a parabolic failure envelope, as shown in Fig. 14(b), taking concrete strength $f_c = 30$ MPa for example.

On the other hand, when failure is initiated by shear, the Mohr circle should be tangent to the Mohr-Coulomb criterion first, as shown in Fig. 15(a). The distance between the center of the stress circle ($\sigma_c/2$, 0) and the line of the Mohr-Coulomb criterion equals the radius of the stress circle, and let $k = \tan\varphi$, it results
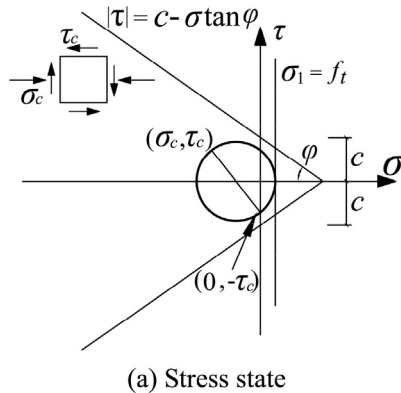
$$\frac{\left|\frac{k}{2}\sigma_c - c\right|}{\sqrt{k^2 + 1}} = \frac{1}{2}\sqrt{4\tau_c^2 + \sigma_c^2} \tag{13}$$
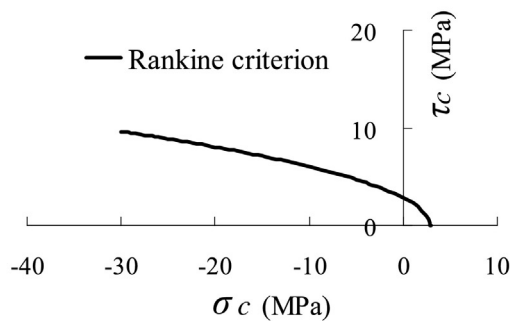
Eq. (13) can be converted into:

$$\left(\frac{\sigma_c + 2kc}{2c\sqrt{k^2 + 1}}\right)^2 + \left(\frac{\tau_c}{c}\right)^2 = 1 \tag{14}$$

The failure envelope of σ_c and τ_c in Eq. (14) is an ellipse, as shown in Fig. 15(b).

The two failure envelopes together determine the final failure pattern of concrete, as shown in Fig. 16. The intersection point of the two envelopes is $(-2kc, c)$. On the left side of the intersection point, where the ratio of $|\sigma_c|$ and τ_c is larger than $2k$, the control criterion is the Mohr-Coulomb envelope. On the right side with the ratio of $|\sigma_c|$ and τ_c less than $2k$, by contrast, the Rankine criterion is more critical. For ordinary concrete the friction angle is usually between 38° and 45°, thus the value of $2k$ lies between 1.5 and 2.0.

4.4.2. Mechanical analysis of the slab sector model

To simplify the problem, an idealized model that an axis-symmetric circular slab subjected to a circular patch load at the center is considered. The stress state in the slab can be represented by the radial segment in Fig. 17, since it is symmetric along the tangential direction. In the sector model, the mechanical behavior and crack pattern is very similar to a one dimensional beam when the angle $\Delta\varphi$ is small enough, except for the existence of the tangential stresses. Some classical theories developed on beams can be used here with proper modifications, and the complex problem can be simplified consequently.

The radial flexural cracks and the tangential diagonal cracks have already existed before the final punching. To cut the sector along the tangential diagonal crack and the vertical section at the tip of the crack, the sector is divided into part I and part II as shown in Fig. 18. Neglecting the contribution from tie bars first, the forces acting on the sector are as follows:

a) The external load or reaction force $P_{cd}\Delta\varphi/2\pi$.
b) The tensile force of the bottom steel plate F_{sr}, and the corresponding compression force C_c provided by the top steel plate and concrete together in the radial direction. The two forces are caused by the radial moment M_r.
c) The tensile force of the bottom steel plate F_{st}, and the corresponding compression force F_{ct} provided by the top steel plate and concrete in the tangential direction, which results from the tangential moment M_t.
d) The dowel shear force V_d in the bottom steel plate.
e) The concrete shear force V_c in the shear-compression zone.

As the model is tangentially symmetric, the radial sections are free from shear forces. The equilibrium of the forces in the x, y directions and the equilibrium of moments around the action point of C_c and V_c gives:

$$\sum F_x = 0 : C_c + F_{ct} \cdot \Delta\phi = F_{st} \cdot \Delta\phi + F_{sr} \tag{15}$$

$$\sum F_y = 0 : P_{cd} \cdot \frac{\Delta\phi}{2\pi} = V_c + V_d \tag{16}$$

$$\begin{aligned}\sum M = 0 : P_{cd} \cdot \frac{\Delta\phi}{2\pi} \cdot [x_c + (h - y_c)\tan\theta] \\ = F_{sr} \cdot (h - y_c/3) + V_d \cdot (h - y_c)\tan\theta\end{aligned} \tag{17}$$

In Eqs. (15)–(17) there are seven unknown forces. Some other conditions should be introduced. The tangential and radial directions are orthogonal and the moments are resisted in the two directions independently. Some classical beam theories are still applicable. For example, the depth of concrete compression zone, y_c, is estimated in RC members
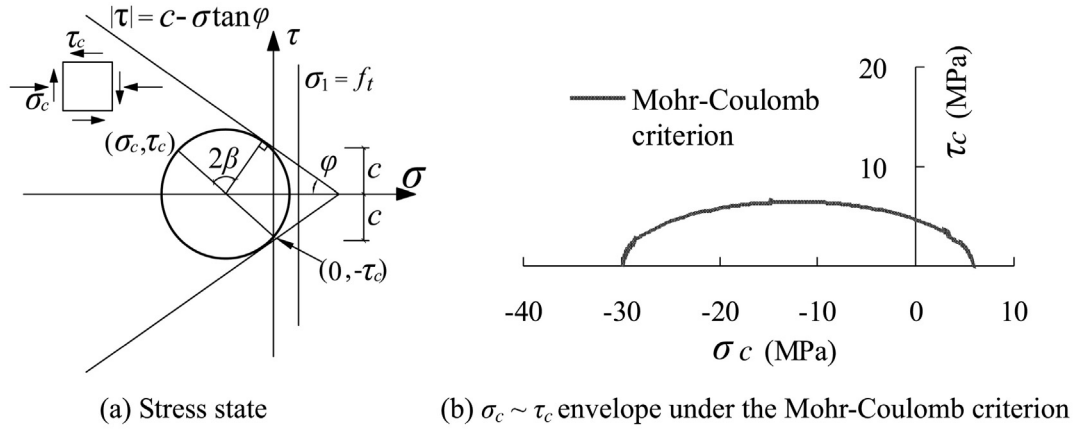

(a) Stress state   (b) $\sigma_c \sim \tau_c$ envelope under the Rankine criterion

Fig. 14. Tension failure under the interaction of σ_c and τ_c.

(a) Stress state   (b) $\sigma_c \sim \tau_c$ envelope under the Mohr-Coulomb criterion

Fig. 15. Shear failure under the interaction of σ_c and τ_c.

[32] as:

$$\left(\frac{y_c}{h}\right)^2 + 600\frac{\rho}{f_c} - 600\frac{\rho}{f_c} = 0 \tag{18}$$

Eq. (18) is obtained from equilibrium and compatibility conditions, in which ρ is the longitudinal reinforcement ratio. But for SCS members with the top steel plate on the very outer surface, the flexural cracks develop much fully. The depth y_c in SCS members, which is thus smaller than that in RC members, is derived in Ref. [17]:

$$\frac{y_c}{h} = \frac{N}{N_1 + 1}, N_1 = \sqrt{\frac{2n\rho}{1 + 2n\rho}} \tag{19}$$

where $\rho = t_s/h$ refers to the steel plate ratio. For SC members with no top steel skin, Eq. (18) is more appropriate.

In the compression zone, the tangential force F_{ct} and radial force C_c both include the contribution from the concrete and top steel plate. Considering the uneven distribution of stresses in this region, the resultant forces are supposed to act not at the center of the compression zone, but nearer to the top steel plate, with a distance about $y_c/3$ from the top surface. For members with common steel ratios, the depth y_c usually ranges from 0.3h to 0.4h, thus the flexural lever arm of both tangential and radial sections can be estimated as $z \approx 0.9h$.

The inclination θ of the diagonal crack in the figure, which is recognized as the last flexural-shear crack before final failure, is also proposed in Ref. [32] with a second-order equation. According to the experimental results, the angle has very limited variations under different conditions, and can further be estimated as $\tan\theta \approx 0.8$.

The position of the diagonal crack x_c is also available theoretically [32]:

$$\frac{x_c}{h} = \left(1 - \frac{y_c}{h}\right) \cdot \left(\frac{a/h}{1 - 0.36y_c/h} - \tan\theta\right) \tag{20}$$

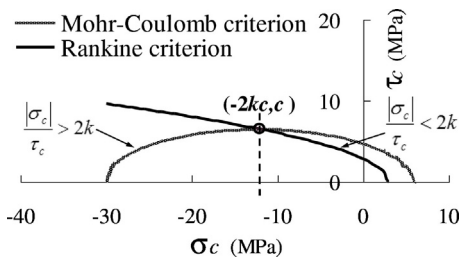On the radial surfaces subjected to pure bending, the tangential moment M_t is available with Eq. (1b). Substituting different values of a, b and r into Eq. (1b), it turns out that the values of M_t just decrease slightly from the center to the support. An estimation of $M_t \approx 0.1P$ will not induce severe deviations. Thus the tangential forces resulting from the tangential moment are derived as:

$$F_{st} = \frac{0.1P}{0.9h} \cdot x_c \tag{21}$$

$$F_{ct} = \frac{0.1P}{0.9h} \cdot (x_c + (h - y_c)\tan\theta) \tag{22}$$

The dowel shear force V_d is related to the tensile force F_{sr}. The opening of the diagonal crack is assumed to be perpendicular to its direction around the tip of the crack [32], as shown in Fig. 19. The compression zone above the crack essentially acts as a buffer, preventing any shear slip along the crack, thus the crack opens orthogonally. The total strain of the bottom steel plate ε_{cr} is perpendicular to the crack, and the corresponding normal strain ε_s and shear strain γ_s can be obtained from a tensoral consideration [32]:

$$\begin{aligned} \varepsilon_s &= \varepsilon_{cr}\cos^2\theta \\ \gamma_s &= \varepsilon_{cr}\sin\theta\cos\theta \end{aligned} \tag{23}$$

The corresponding steel stresses are $\sigma_s = E_s \cdot \varepsilon_s$, and $\tau_s = G_s \cdot \gamma_s$. Considering the approximate relation between the elastic modulus E_s and shear modulus G_s that $G_s \approx 0.4E_s$, the relation between V_d and F_{sr} is

$$V_d = 0.4F_{sr}\tan\theta \tag{24}$$

with the increase of shear span/depth ratio, the value of F_{sr} increases correspondingly, but the value V_d may not increase proportionally, since in slender members, the rotation efficiency of part II is limited by
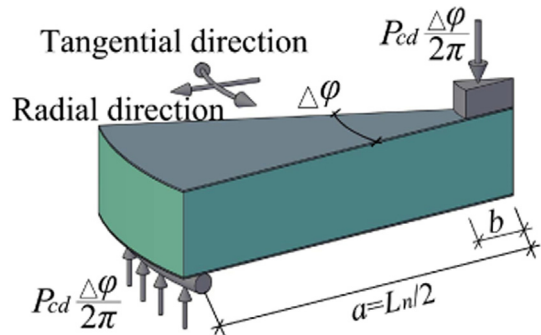

Fig. 16. Failure envelopes of concrete under the interaction of σ_c and τ_c.

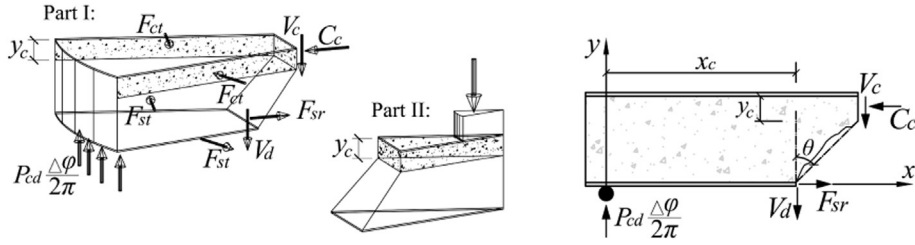**Fig. 17.** The radial sector model.

Fig. 18. Internal forces acting on the slab sector.

interfacial slippage and separation. Consequently, the value of V_d is limited with [32]:

$$V_d = \min\left[0.4F_{sr}\tan\theta, \left(1-\frac{y_c}{h}\right)/\left(1-\frac{1}{3}\frac{y_c}{h}\right)P\cdot\frac{\Delta\phi}{2\pi}\right] \quad (25)$$

Taking Eqs. (21)–(22) and Eq. (25) into Eqs. (15)–(17), it results

$$C_c = \left[\frac{x_c+(h-y_c)\tan\theta}{0.9h+0.4\tan^2\theta(h-y_c)}-2\pi\cdot0.11\tan\theta\left(1-\frac{y_c}{h}\right)\right]P_{cd}\cdot\frac{\Delta\phi}{2\pi} \quad (26)$$

$$V_c = \left[1-0.4\tan\theta\frac{x_c+(h-y_c)\tan\theta}{0.9h+0.4\tan^2\theta(h-y_c)}\right]P_{cd}\cdot\frac{\Delta\phi}{2\pi} \quad (27)$$

The radial compression force C_c consists of the contribution from the steel plate and concrete, while the radial shear force V_c is mainly undertaken by the concrete, since the concrete compression zone prevents the vertical shear deformation of the top steel plate. Taking the values of y_c、x_c and $\tan\theta$ into Eqs. (26)–(27), the values of C_c and V_c are directly related to the external load P_{cd}. And the normal and shear stresses of the critical section (the section around the loading perimeter) are:

$$\sigma_c = -\frac{C_c}{\Delta\phi(y_c/h+n\rho)\cdot bh};\tau_c = \frac{V_c}{\Delta\phi\cdot by_c} \quad (28)$$

From the calculation results, the value of $|\sigma_c|/\tau_c$ is greater than 2.0 when shear span/depth ratio exceeds 1.5, which means that in ordinary slender slabs, punching shear is initiated from shear-compression failure of concrete in the compression zone. The control criterion is the Mohr-Coulomb criterion, according to Fig. 16.

Taking σ_c and τ_c into the Mohr-Coulomb criterion in Eq. (14), the external load P_{cd} can be solved from the second-order equation. The force P_{cd} consists of the shear forces of the concrete (V_c) and steel plate (V_d). Shear punching failure of SCS slabs is essencially resulting from shear failure of concrete in the compression zone around the loading
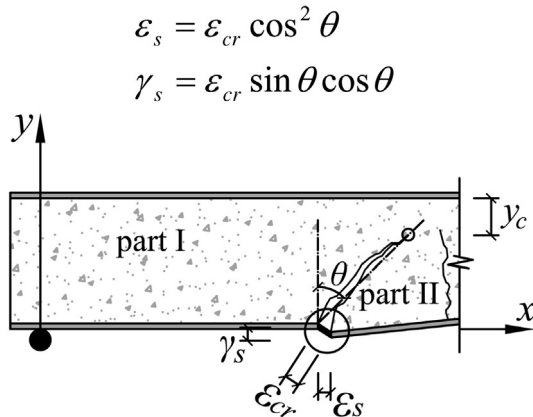
perimeter, which is the most critical location of both maximum shear and bending moment, but with minimum section area.

For SC slabs without top steel plates, the force transfer mechanism, equilibrium equations and failure criterion are the same with that in SCS members, except that the action of the top steel plate is removed. So the normal stress is modified into $\sigma_c = -C_c/(\Delta\varphi\cdot y_ch)$, and other expressions are all the same.

4.4.3. Shear contribution of the tie bars.

The tie bars will directly contribute to the punching shear capacity when they are passed through by the diagonal cracks. Strain gauges were attached to some of the tie bars in specimen B-1-4 × 3.5 to study the tensile stresses of the tie bars at different positions, as shown in Fig. 20. The black dots were the array of the tie bars, and a total of 14 bars, amplified in the figure, were installed with strain gauges at the center. The strain gauges were attached to the bars before welding, and protected with waterproof adhesive. The two perimeters around the loading region for reference, marked as A and B, are located with a distance h and 2 h respectively from the load edge. The middle of each side of the referential perimeter is parallel and of equal length to the loading perimeter, and the corner is arc-shaped. Such a perimeter is similar to the outline of the bulge observed in the tests, and is also suggested as the shape of the critical punching perimeter by Eurocode 2 [29].

Fig. 21 illustrates the relationship between the external load P and tensile strains of each tie bar. The strains increased regularly with the development of tangential diagonal cracks. The bars were not stressed before the formation of the diagonal cracks. Between 600 kN and 1200 kN the strains of TB1, TB5 and TB10 began to increase, followed
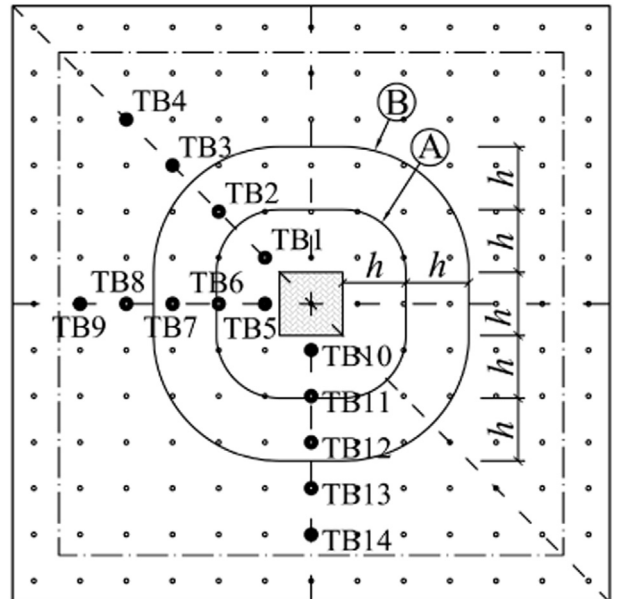
$$\varepsilon_s = \varepsilon_{cr}\cos^2\theta$$
$$\gamma_s = \varepsilon_{cr}\sin\theta\cos\theta$$

Fig. 19. Deformation after diagonal cracking.

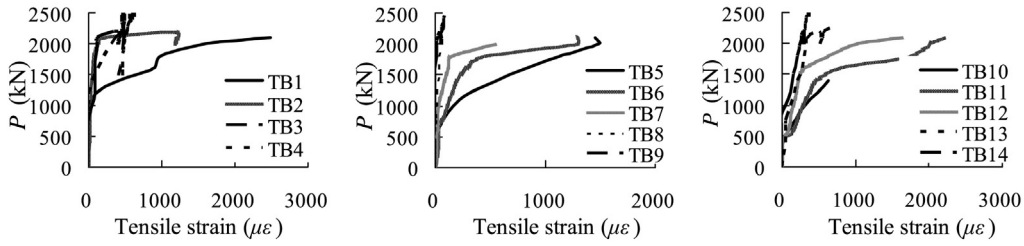**Fig. 20.** Strain gauges on the tie bars in specimen B-1-4 × 3.5.

Fig. 21. Tensile strains of the tie bars in specimen B-1-4 × 3.5.

by TB6 and TB11. At 2200 kN when punching occurred in concrete, the strains of TB2, TB7 and TB12 increased dramatically. Some of the strain gauges were even destroyed or overranged once cracks passed through. The tie bars outside the perimeter B, i.e., TB3, TB4, TB8, TB9, TB13 and TB14, were not stressed even after punching. It indicates that the bottom face of the punching cone is close to perimeter B, with a distance about 2h from the load edge, and the inclination angle of the critical punching crack is about 26°.

In specimens with relatively thick steel skins, the tie bars will fail at the cracked position. But there is another possibility that the tie bar may fails by steel skins shear fractured around the bar perimeter, which actually happened in the specimens with 3 mm steel plates in the tests. Therefore, the tensile capacity of a tie bar can be estimated as the lower of 1) the tensile strength of the tie bar itself and 2) the shear strength of the steel plate around the bar:

$$T_{svi} = \min\left(A_{sv1}f_{yv}, \frac{f_y}{\sqrt{3}} \cdot \pi d_v \cdot t_s\right) \quad (29)$$

in which A_{sv1}, d_v and f_{yv} are the cross section area, diameter and yield strength of the tie bar; f_y and t_s are the yield strength and thickness of the steel plate.

At the punching moment, the tie bars between the load edge and the perimeter A have yielded generally, but the tie bars between A and B have partially yielded, not entirely. The strength of the tie bars are not

developed simultaneously. From the experimental data, it is a reasonable estimation to consider the contribution of 1) all the tie bars between the load edge and perimeter A and 2) 1/3 of the tie bars between A and B. The periphery A and B are sketched in Fig. 20. The shear contribution of the tie bars to the punching strength can be estimated as:

$$V_{sv,cr} = T_{svi}(n_1 + n_2/3) \quad (30)$$

or

$$V_{sv,cr} = \frac{T_{svi}}{b_x b_y}\left(5.33bh + 2\pi h^2\right) \quad (31)$$

The subscript '*cr*' refers to the state of punching failure of the concrete, as distinguished from the ultimate state. n_1 and n_2 refer to the number of the tie bars between the load edge and the perimeter A, and between A and B, respectively. The expression in the bracket in Eq. (31) equals the plane area of the perimeter A subtracting the loading area, added with 1/3 the area between A and B.

4.4.4. Punching shear capacity

The punching shear capacity of SCS slabs consists of the resistances of the concrete and steel plate, as well as the tie bars across the shear crack. The contribution of the tie bars, $V_{sv,cr}$, can be calculated according
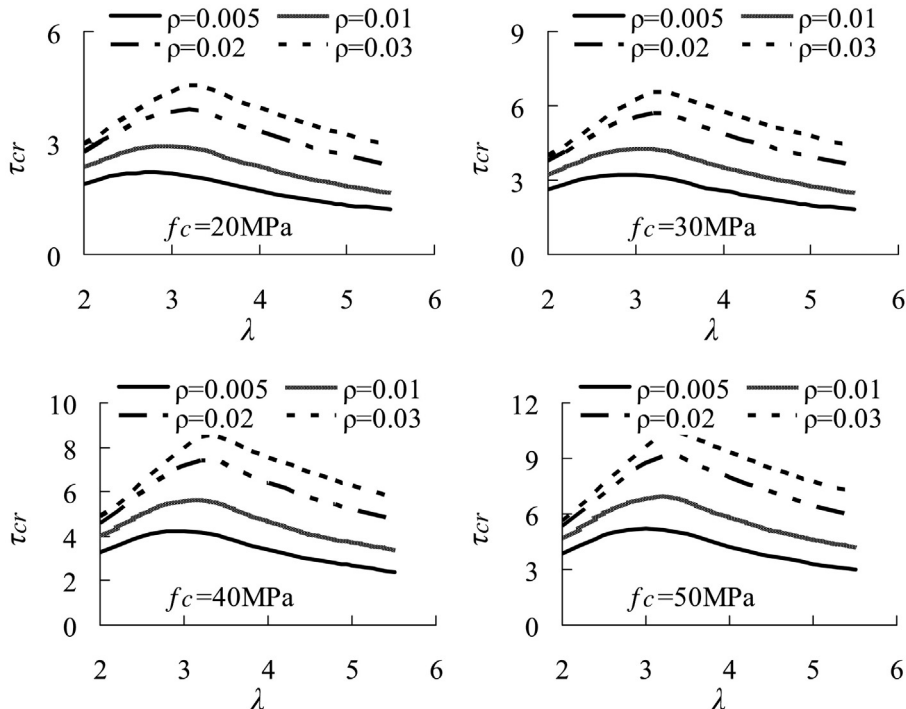

Fig. 22. Punching shear strength τ_{cr} of SCS slabs.

Table 3
Comparisons between calculated and tested strengths.

Specimen	Flexural strength P_f				Punching shear strength P_{cr}					Ultimate strength P_u			
	m_f (kN·m/m)	P_{f_cal} (kN)	P_{f_exp} (kN)	$\frac{P_{f\,cal}}{P_{f\,exp}}$	τ_{cr} (MPa)	$V_{sv,cr}$ (kN)	P_{cr_cal} (kN)	P_{cr_exp} (kN)	$\frac{P_{cr\,cal}}{P_{cr\,exp}}$	$V_{sv,u}$ (kN)	P_{u_cal} (kN)	P_{u_exp} (kN)	$\frac{P_{u\,cal}}{P_{u\,exp}}$
D-1-4 × 2.35	124	1314	\	\	6.011	19	630	596	1.058	255	751	730	1.029
D-1-4 × 3.7	124	1135	\	\	5.499	191	593	670	0.885	255	751	780	0.963
DH-1-4 × 2.35	112	1191	\	\	5.881	0	429	450	0.954	\	\	\	\
DH-1-4 × 3.7	112	1029	\	\	6.034	0	441	539	0.817	\	\	\	\
B-1-4 × 3.5	454	4153	\	\	6.230	433	2194	2200	0.997	625	2454	2480	0.990
D-1-4 × 6	124	1119	1030	1.087	\	\	\	\	\	446	1407	1390	1.012

to Eq. (30) or Eq. (31). The resistances of concrete, V_c, and steel plate, V_d, are correlated as part of the external load P_{cd}, as shown in Fig. 18. The value of P_{cd} can be solved by substituting Eqs. (26)–(28) into the Mohr-Coulomb criterion in Eq. (14), which is a second-order equation. As P_{cd} is a function of shear span/depth ratio λ, steel plate ratio ρ, and concrete strength f_c, it can be expressed graphically for convenience. Define a nominal punching shear strength τ_{cr} as:

$$\tau_{cr} = P_{cd}/2\pi bh \tag{32}$$

The values of τ_{cr} for different λ, ρ, and f_c are shown in Fig. 22, and the punching shear capacity P_{cr} is obtained with

$$P_{cr} = \tau_{cr} \cdot 2\pi bh + V_{sv,cr} \tag{33}$$

in which $2\pi b$ refers to the loading perimeter. Eq. (33) is derived from the idealized axis-symmetric slab sector model. In practice the situation is rarely perfectly axis-symmetric, but the force mechanism and failure criterion are identical. Eq. (33) is still applicable. In rectangular slabs subjected to a rectangular patch load, the loading perimeter can be replaced by $\pi(b_1 + b_2)/2$, where b_1 and b_2 refer to the lengths of the perpendicular sides of the loading region. The equivalent circular loading perimeter, rather than the actual one is adopted to consider the nonuniform distribution of stresses along the loading perimeter.

4.5. Ultimate capacity P_u

After flexural yielding or concrete punching, the carrying capacity rises gradually until shear failure of the top steel plate. During this process the action of the top steel plate is fully developed under large deflections. So the ultimate capacity P_u is dependent mainly on the shear capacity of the top steel plate, as well as the tie bars across the diagonal cracks. The ultimate capacity can be calculated as:

$$P_u = \frac{f_u}{\sqrt{3}} \cdot c_p t_s + V_{sv,u} \tag{34}$$

f_u is the ultimate strength of the top steel plate, and c_p is the loading perimeter, along which the plate is sheared off. During the loading process from P_{cr} or P_f to P_u, some of the tie bars, especially within the perimeter A, have been tensile fractured. During the tests, the fracture of the tie bars was visible from the outside in specimens with 3 mm steel plates, as the fracture position is around the steel skins. The contribution of the tie bars at the ultimate state, denoted with the subscript 'u', can therefore be approximated as the total strength of the bars distributed between perimeters A and B:

$$V_{sv,u} = n_2 T_{svi} = \frac{T_{svi}}{b_x b_y}\left(4bh + 3\pi h^2\right) \tag{35}$$

4.6. Experimental verification

The punching shear capacity P_{cr}, flexural capacity P_f and ultimate capacity P_u are calculated with the proposed method and compared with the test results in Table 3. The measured material strengths are used. In Table 3 the subscripts '$\_cal$' and '$\_exp$' refer to the calculated and experimental values respectively. For the flexural capacity P_f, the upper bound solution from the yield line theory is slightly larger than the actual yield point in specimen D-1-4 × 6. Other specimens failed by shear punching. In the SC specimens without top steel plate, the method underestimates the punching shear capacities. It may be due to the dowel effect of the longitudinal steel bars, which is ignored in the model. For the ultimate capacity P_u, the calculated capacities all coincide well with the tested values. In contrast, the prediction of the concrete punching strength P_{cr} shows more uncertainty. In general, the mechanical model gives reasonable predictions of the flexural and punching capacities of SCS sandwich slabs under concentrate loads.

5. Conclusions

This paper focuses on the mechanical behavior of SCS sandwich slabs. Six simply supported steel-concrete-steel (SCS) or steel-concrete (SC) composite slabs were tested under concentrate loads applied at the center. Shear span/depth ratios and section depths varied among the specimens. The global and local deformations, strains of the steel skins and tie bars were measured during the tests. Concrete cracks were visualized after testing by partially taking off the steel skins.

From the test results, the failure modes can be basically recognized as flexural yielding and shear punching. Some potential local damage patterns like local buckling and interfacial slippage are not considered presently. In the tests of SCS slabs both failure patterns showed excellent ductile behavior, which were attributed to the shear contribution and membrane action of the steel skins. These effects were even more evident under large deflections. The shear contribution of the top steel plate and tie bars was confirmed from the comparisons between SCS and SC specimens.

Flexural failure was characterized by tensile yielding of the bottom steel plate and the global flexural deformed shape. Yielding initiated from the load vicinity and gradually progressed throughout the whole span. An upper bond solution dealing with the flexural capacity was derived with the classical yield-line method.

Punching shear failure was characterized by punching of the concrete core and the local bulge around the load vicinity. Inclination of the punching cone surface was about 26°–30°. The punching shear capacities and ultimate capacities were discussed analytically. The punching shear capacity P_{cr} was studied in depth, with the mechanical analysis on the radial sector model and the concrete failure criteria. And the ultimate capacity P_u was dependent primarily on the shear capacity of the top steel plate around the load perimeter. The shear contribution of the tie bars was also discussed.

The proposed method can accurately predict the capacities of SCS slabs, and reflect the force mechanism of different failure patterns.

Acknowledgements

References

[1] K.M.A. Sohel, J.Y.R. Liew, J.B. Yan, M.H. Zhang, K.S. Chia, Behavior of steel-concrete-steel sandwich structures with lightweight cement composite and novel shear connectors, Compos. Struct. 94 (12) (2012) 3500–3509.

[2] J.Y.R. Liew, K.M.A. Sohel, C.G. Koh, Impact tests on steel-concrete-steel sandwich beams with lightweight concrete core, Eng. Struct. 31 (9) (2009) 2045–2059.

[3] S.K. Solomon, D.W. Smith, A.R. Cusens, Flexural tests of steel–concrete–steel sandwiches, Mag. Concr. Res. 28 (94) (1976) 13–20.

[4] M. Tomlinson, A. Tomlinson, M. Chapman, H.D. Wright, A.D. Jefferson, Shell composite construction for shallow draft immersed tube tunnels, Proceedings of the ICE International Conference on Immersed Tube Tunnel Techniques, Manchester (UK), Thomas Telford, April 1989.

[5] H. Bowerman, N. Coyle, J.C. Chapman, An innovative steel/concrete construction system, J. Struct. Eng. 80 (20) (2002) 33–38.

[6] J.Y.R. Liew, K.M.A. Sohel, Lightweight steel-concrete-steel sandwich system with J-hook connectors, Eng. Struct. 31 (5) (2009) 1166–1178.

[7] T.M. Roberts, D.N. Edwards, R. Narayanan, Testing and analysis of steel-concrete-steel sandwich beams, J. Constr. Steel Res. 38 (3) (1996) 257–279.

[8] T.O.S. Oduyemi, H.D. Wright, An experimental investigation into the behaviour of double-skin sandwich beams, J. Constr. Steel Res. 14 (3) (1989) 197–220.

[9] H.D. Wright, T.O.S. Oduyemi, H.R. Evans, The experimental behaviour of double skin composite elements, J. Constr. Steel Res. 19 (2) (1991) 97–110.

[10] B. McKinley, L.F. Boswell, Behaviour of double skin composite construction, J. Constr. Steel Res. 58 (10) (2002) 1347–1359.

[11] M. Xie, N. Foundoukos, J.C. Chapman, Static tests on steel–concrete–steel sandwich beams, J. Constr. Steel Res. 63 (6) (2007) 735–750.

[12] J.Y.R. Liew, K.M.A. Sohel, Structural performance of steel-concrete-steel sandwich composite structures, Adv. Struct. Eng. 13 (3) (2010) 453–470.

[13] S.K. Clubley, S.S.J. Moy, R.Y. Xiao, Shear strength of steel-concrete-steel composite panels. Part I – testing and numerical modeling, J. Constr. Steel Res. 59 (6) (2003) 781–794.

[14] S.K. Clubley, S.S.J. Moy, R.Y. Xiao, Shear strength of steel-concrete-steel composite panels. Part II – detailed numerical modeling of performance, J. Constr. Steel Res. 59 (6) (2003) 795–808.

[15] Y.B. Leng, X.B. Song, M. Chu, H.H. Ge, Experimental study and theoretical analysis on resistance of steel-concrete-steel sandwich beams, J. Struct. Eng. 141 (2) (2015) 04014113.

[16] Y.B. Leng, X.B. Song, H.L Wang, Failure mechanism and shear strength of steel-concrete-steel sandwich deep beams, J. Constr. Steel Res. 106 (2015) 89–98.

[17] Y.B. Leng, X.B. Song, Experimental study on shear performance of steel–concrete–steel sandwich beams, J. Constr. Steel Res. 120 (2016) 52–61.

[18] N.E. Shanmugam, G. Kumar, V. Thevendran, Finite element modelling of double skin composite slabs, Finite Elem. Anal. Des. 38 (7) (2002) 579–599.

[19] K.M.A. Sohel, J.Y.R. Liew, Steel-concrete-steel sandwich slabs with lightweight core – static performance, Eng. Struct. 33 (3) (2011) 981–992.

[20] J.B. Yan, J.Y. Wang, J.Y.R. Liew, X.D. Qian, Z.X. Li, Punching shear behavior of steel–concrete–steel sandwich composite plate under patch loads, J. Constr. Steel Res. 121 (2016) 50–64.

[21] J.B. Yan, J.Y. Wang, J.Y.R. Liew, X.D. Qian, L. Zong, Ultimate strength behaviour of steel–concrete–steel sandwich plate under concentrated loads, Ocean Eng. 118 (2016) 41–57.

[22] J.B. Yan, J.Y.R. Liew, Design and behaviour of steel-concrete-steel sandwich plates subject to concentrated loads, Compos. Struct. 150 (2016) 139–152.

[23] G.I.B. Rankin, A.B. Long, Predicting the punching strength of conventional slab–column specimen, Proc. Inst. Civ. Eng. (London) 82 (1987) 327–346.

[24] S. Kinnunen, H. Nylander, Punching of concrete slabs without shear reinforcement, Trans. of the Royal Institute of Technology, No. 158, Stockholm, Sweden, 1960.

[25] A. Muttoni, M.F. Ruiz, Shear strength of members without transverse reinforcement as function of critical shear crack width, ACI Struct. J. 105 (2) (2008) 163–172.

[26] A. Muttoni, Punching shear strength of reinforced concrete slabs without transverse reinforcement, ACI Struct. J. 105 (4) (2008) 440–450.

[27] D.H. Jiang, J.H. Shen, Strength of concrete slabs in punching shear, J. Struct. Eng. 112 (12) (1986) 2578–2591.

[28] A.E. Long, D. Bond, Punching failure of reinforced concrete slabs, Proc. Inst. Civ. Eng. (London) 39 (1) (1967) 109–135.

[29] European Committee for Standardization, Design of concrete structures – part 1–1: general rules and rules for buildings, Eurocode 2, Brussels, 1992.

[30] W.F. Chen, A.F. Saleeb, Elasticity and Plasticity [M], China Architecture & Building Industry Press, Beijing, 2004.

[31] Z.X. Zha, X.L. Liu, W. Peng, B. Xu, Cracking patterns of shear walls in reinforced concrete structure due to strong earthquake based on Mohr-Coulomb criterion, J. Donghua Univ. (Eng. Ed.) 32 (4) (2015) 541–548.

[32] P.D. Zararis, G.C. Papadakis, Diagonal shear failure and size effect in RC beams without web reinforcement, J. Struct. Eng. 127 (7) (2001) 733–742.